

# Soft, curved electrode systems capable of integration on the auricle as a persistent brain–computer interface

James J. S. Norton<sup>a</sup>, Dong Sup Lee<sup>b,c</sup>, Jung Woo Lee<sup>d,e</sup>, Woosik Lee<sup>c</sup>, Ohjin Kwon<sup>c</sup>, Phillip Won<sup>d</sup>, Sung-Young Jung<sup>d,f</sup>, Huanyu Cheng<sup>g</sup>, Jae-Woong Jeong<sup>h</sup>, Abdullah Akce<sup>i</sup>, Stephen Umunna<sup>j</sup>, Ilyoun Na<sup>d,k</sup>, Yong Ho Kwon<sup>d</sup>, Xiao-Qi Wang<sup>l</sup>, Zhuangjian Liu<sup>m</sup>, Ungyu Paik<sup>e</sup>, Yonggang Huang<sup>g</sup>, Timothy Bretl<sup>n</sup>, Woon-Hong Yeo<sup>c,1</sup>, and John A. Rogers<sup>d,1</sup>

<sup>a</sup>Neuroscience Program, University of Illinois at Urbana-Champaign, Urbana, IL 61801; <sup>b</sup>Department of Chemical and Life Science Engineering, Virginia Commonwealth University, Richmond, VA 23284; <sup>c</sup>Department of Mechanical and Nuclear Engineering, Center for Rehabilitation Science and Engineering, Virginia Commonwealth University, Richmond, VA 23284; <sup>d</sup>Department of Materials Science and Engineering, University of Illinois at Urbana-Champaign, Urbana, IL 61801; <sup>e</sup>Department of Materials Science and Engineering, Department of Energy Engineering, Hanyang University, Seoul 133-791, Republic of Korea; <sup>f</sup>Department of Mechanical Engineering, Pohang University of Science and Technology, Pohang 790-784, Republic of Korea; <sup>g</sup>Departments of Civil and Environmental Engineering and Mechanical Engineering, Center for Engineering and Health, Skin Disease Research Center, Northwestern University, Evanston, IL 60208; <sup>h</sup>Department of Electrical, Computer, and Energy Engineering, University of Colorado Boulder, Boulder, CO 80309; <sup>i</sup>Google Inc., Mountain View, CA 94043; <sup>j</sup>Department of Molecular and Integrative Physiology, University of Illinois at Urbana-Champaign, Urbana, IL 61801; <sup>k</sup>Department of Chemical Engineering, Pohang University of Science and Technology, Pohang 790-784, Republic of Korea; <sup>l</sup>Department of Dermatology, Feinberg School of Medicine, Northwestern University, Chicago, IL 60611; <sup>m</sup>Institute of High Performance Computing, 138632, Singapore; and <sup>n</sup>Department of Aerospace Engineering, University of Illinois at Urbana-Champaign, Urbana, IL 61801

Edited by Zhenan Bao, Stanford University, Stanford, CA, and accepted by the Editorial Board February 17, 2015 (received for review December 31, 2014)

**Recent advances in electrodes for noninvasive recording of electroencephalograms expand opportunities collecting such data for diagnosis of neurological disorders and brain–computer interfaces. Existing technologies, however, cannot be used effectively in continuous, uninterrupted modes for more than a few days due to irritation and irreversible degradation in the electrical and mechanical properties of the skin interface. Here we introduce a soft, foldable collection of electrodes in open, fractal mesh geometries that can mount directly and chronically on the complex surface topology of the auricle and the mastoid, to provide high-fidelity and long-term capture of electroencephalograms in ways that avoid any significant thermal, electrical, or mechanical loading of the skin. Experimental and computational studies establish the fundamental aspects of the bending and stretching mechanics that enable this type of intimate integration on the highly irregular and textured surfaces of the auricle. Cell level tests and thermal imaging studies establish the biocompatibility and wearability of such systems, with examples of high-quality measurements over periods of 2 wk with devices that remain mounted throughout daily activities including vigorous exercise, swimming, sleeping, and bathing. Demonstrations include a text speller with a steady-state visually evoked potential-based brain–computer interface and elicitation of an event-related potential (P300 wave).**

soft electronics | auricle integration | brain–computer interface | text speller

For more than 80 y, electroencephalography (EEG) has provided an effective noninvasive means to study human brain activity (1). EEG is instrumental in a wide range of clinical and research applications, from diagnosing epilepsy (2) to improving our understanding of language comprehension (3) and the development of brain–computer interfaces (BCI) (4). Conventional EEG recording systems, particularly the physical interface between the sensor (commonly known as an electrode) and the head, have limitations that constrain the more widespread use of EEG monitoring. Electrodes typically consist of rigid metal disks mechanically secured to the head with a mesh cap and chin strap, where electrolyte gels (5) enable efficient electrical coupling by reducing the impedance at the skin interface. This arrangement causes skin irritation (erythema) and leads to electrical degradation for periods of use that extend more than a few hours, typically caused by drying of the electrolyte gel (6). Recent technologies replace the gel (7, 8) with needles (8, 9), contact probes (10, 11), capacitive disks (12, 13), conductive composites (14, 15), or nanowires (16). Such dry electrodes have some

promise, but they require multistep preparations, obtrusive wiring interfaces, and/or cumbersome mechanical fixtures. These shortcomings limit the potential for long-term use in diagnosis of neurological disabilities (17, 18) or in persistent BCI (17, 19). For example, although microneedle electrodes can record EEG signals for a few hours (20), the interface does not offer the robustness, comfort, or ease of use needed for sustained operation. Capacitive electrodes that incorporate thin, reversible adhesives to the surface of the scalp avoid some of these drawbacks, but current designs involve bulky rigid electrode structures with thicknesses in the range of several millimeters (21). Although long-term EEG recordings are possible, this device construction (21) is susceptible to mechanically induced delamination, such that it cannot remain mounted during bathing, and it must be physically protected during sleep. Improved versions offer shapes that allow insertion into the ear canal (22) but in a way that obstructs hearing while retaining some of the other disadvantages of the

## Significance

Conventional electroencephalogram (EEG) recording systems, particularly the hardware components that form the physical interfaces to the head, have inherent drawbacks that limit the widespread use of continuous EEG measurements for medical diagnostics, sleep monitoring, and cognitive control. Here we introduce soft electronic constructs designed to intimately conform to the complex surface topology of the auricle and the mastoid, to provide long-term, high-fidelity recording of EEG data. Systematic studies reveal key aspects of the extreme levels of bending and stretching that are involved in mounting on these surfaces. Examples in persistent brain–computer interfaces, including text spellers with steady-state visually evoked potentials and event-related potentials, with viable operation over periods of weeks demonstrate important advances over alternative brain–computer interface technologies.

Author contributions: J.J.S.N., U.P., Y.H., W.-H.Y., and J.A.R. designed research; J.J.S.N., D.S.L., J.W.L., W.L., O.K., P.W., S.-Y.J., H.C., J.-W.J., A.A., S.U., I.N., Y.H.K., X.-Q.W., Z.L., and W.-H.Y. performed research; J.J.S.N., T.B., W.-H.Y., and J.A.R. analyzed data; and J.J.S.N., D.S.L., T.B., W.-H.Y., and J.A.R. wrote the paper.

The authors declare no conflict of interest.

This article is a PNAS Direct Submission. Z.B. is a guest editor invited by the Editorial Board.

<sup>1</sup>To whom correspondence may be addressed. Email: jrogers@illinois.edu or whyeo@vcu.edu.

This article contains supporting information online at [www.pnas.org/lookup/suppl/doi:10.1073/pnas.1424875112/-DCSupplemental](http://www.pnas.org/lookup/suppl/doi:10.1073/pnas.1424875112/-DCSupplemental).



has an effective modulus lower than that of the skin ( $\sim 130$  kPa) (26), to ensure conformal contact (27) and robust adhesion (28). The fabrication procedures can be found in *SI Appendix, Note 1 and Figs. S2–S5*.

A critical feature of the mechanics appears in Fig. 1*B*, which shows a device wrapped onto the triangular fossa, crura of antihelix, and lobule of the ear as well as the mastoid. The ability to adopt the complex surface textures of all areas of the auricle is unique to this class of ultrathin, extremely bendable electronics, largely unexplored in previous reports (26, 29–32). Mounting of the device begins with removal of hair using a razor (Gillette), if necessary, followed by mild rubbing of the auricle area using a sterile alcohol pad (Dukal Corporation) to clean the surface. Electrodes and interconnects are manually placed on the desired locations by using plastic tweezers (Ted Pella, Inc.). Soft bonding from van der Waals interactions holds the device on the skin. Gently spraying water onto the device dissolves the polymer backing layer [polyvinyl alcohol (PVA); Haining Sprutop Chemical Tech] and leaves the soft, ultrathin elastomer in contact with the skin. Careful device handling and complete dissolution of the polymer backing are important to successful mounting. The main consequence of improper mounting is high background noise in the EEG data (*SI Appendix, Fig. S6*).

The magnified image in Fig. 1*B* illustrates how the stretchable interconnects maintain contact with the skin (antihelix) by conforming to the uneven surfaces. These behaviors follow from exceptional levels of both bendability and stretchability, as revealed by finite element method (FEM) analysis. Fig. 1*C* shows FEM results for bending and folding, where the bend angle is  $180^\circ$  and the radius of curvature is 0.5 mm. The maximum principal strain in the metal layers is only 0.25% (elastic limit of Au: 0.3%) (25). Additional results in Fig. 1*D* show mechanical bending simultaneously along two orthogonal axes with relevant radii of curvature (10 mm; comparable to the distance between the tragus and outer edge of the ear) and diameters (1 mm; comparable to the thickness of the ear lobule). The experimental observations (Fig. 1*E–H*) are consistent with the predicted responses, as illustrated by capabilities for mounting and wrapping on the ear. Further FEM analysis under uniaxial tensile loads (*SI Appendix, Fig. S7*) indicates that the electrodes and interconnects can be stretched by up to  $\sim 50\%$ . These results suggest an ability to accommodate larger than average skin deformation (10–20%) (26, 27) up to

and including the maximum strains ( $\sim 50\%$ ) associated with motion of the knee joint (*SI Appendix, Fig. S8*).

This auricle-mounted system can be used in a sequential process for recording and interpreting EEG signals for BCI (Fig. 1*I*). Standard EEG signals such as alpha rhythms can be readily captured (*SI Appendix, Fig. S9*). The three electrodes including the REC (mastoid), REF (upper antihelix), and GND electrode (earlobe) form a bipolar montage. This setup measures the differential amplitudes (REC and REF), and the GND prevents nonspecific, parasitic signals from the body. In addition to a soft, dry interface to the skin and an ability to conform to the auricle, a key point of interest is the related capabilities for long-term use.

The epidermal electrode incorporates well-characterized, biocompatible materials [silicone (25), gold (33), and polyimide (34)]. Studies using keratinocyte cells demonstrate biocompatibility, as shown in Fig. 2*A–E*. Fluorescence microscope images compare the status of cultured cells in three categories: live, injured, and dead by using a cell viability assay (Life Technologies) (Fig. 2*A* and *B*). The numbers of live cells grown on a device and on a control (cell culture Petri dish) are identical within statistical uncertainties. Directly relevant studies involve devices mounted onto subjects for comparative assessments using infrared thermography (35, 36). Data indicate no adverse effects up to 2 wk (Fig. 2*C* and *D*), where a thin overcoat of spray-on-bandage material (3M) ensures survivability during normal daily activities, such as exercising, showering, or swimming. Conventional gel electrodes, by contrast, show clear signs of erythema (elevated temperature in Fig. 2*E*) after 1 d. Furthermore, the gels exhibit a  $\sim 50\%$  reduction in volume due to evaporative drying over 6 h (*SI Appendix, Fig. S10*), consistent with the previous observations (19, 37, 38) of significant increases (2–4 times) in skin–electrode impedance due to the gel dehydration (within 6 h). Evaluations used gel electrodes mounted on a skin replica (polydimethylsiloxane; Dow Corning), placed on a hot plate (Super-Nuova; Thermo Scientific) to mimic the human skin (temperature:  $\sim 37^\circ\text{C}$ ). These and other drawbacks render such conventional gel electrodes unsuitable for continuous, long-term use.

The results in Fig. 3 establish that the long-term epidermal (LTE) electrodes presented here offer fidelity in EEG measurement that compares favorably to that of conventional electrodes. The main advantage of the LTE technology is in its long-term utility, as demonstrated in recordings using electrical connections established in reversible fashion at the peripheral pad terminations of the Peano fractal interconnects (*SI Appendix, Figs. S11 and S12*). The mechanically compliant, reversible interactions facilitated by van der Waals forces provide low electrical resistance for EEG recording. Before the electrical connection, gentle rubbing with a sterile alcohol pad cleans the surface of the pad and connector. A portable, compact microscope (AnMo Electronics) enables exact positioning of the connector. During the course of the experiments, involving multiple cycles of measurements, we observed no significant degradation of the connector. Rather, eventual failure of the system occurs due to peeling of the device electrodes from the skin, likely associated with accumulation of exfoliated cells from the stratum corneum.

A thin layer ( $\sim 1\ \mu\text{m}$ ) of spray-on bandage, applied once or twice a day, facilitates strong bonding to the skin and provides environmental protection (27). Bipolar EEG recordings collected at various time points during 2 d (recording of P300, as described in a subsequent section) and 2 wk (recording of alpha rhythms) with normal living behaviors such as working, exercising, or showering illustrate the electronic viability. Qualitative monitoring by contact microscopy reveals no adverse effects such as rashes, redness, or allergic reactions (*SI Appendix, Fig. S13*). Fig. 3*A* and *B* shows P300 data collected over 24 h on the skin (mastoid and forehead). The signal-to-noise (SNR) ratio corresponds to the ratio of the signal power (from target) to the noise power (from nontarget). The SNR values for these two cases are nearly identical, and they are comparable to the signals obtained

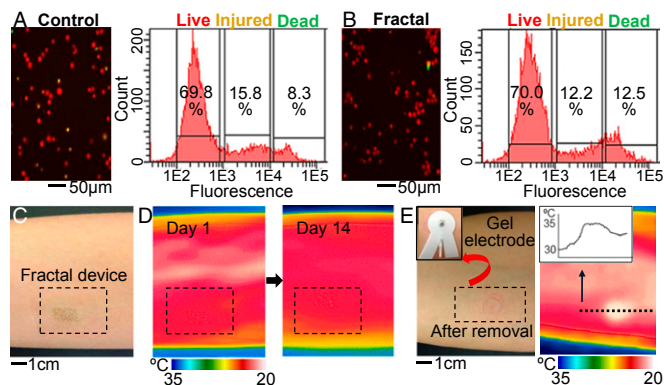


**Fig. 2.** Assessments of biocompatibility by infrared thermography (IRT) and through cell-based studies. (A) Keratinocytes cultured on a control (Petri dish) with fluorescence microscopic image (*Left*) and quantitative measurement of cell viability (*Right*). (B) Keratinocytes cultured on a fractal device for comparison. (C) Image of a fractal device mounted on the forearm. (D) IRT images of the skin surface collected during 2 wk reveal no adverse effects. (E) Image of a gel electrode removed after 1 d (*Left*) and IRT image showing erythema, elevated temperature on the skin (*Right*).

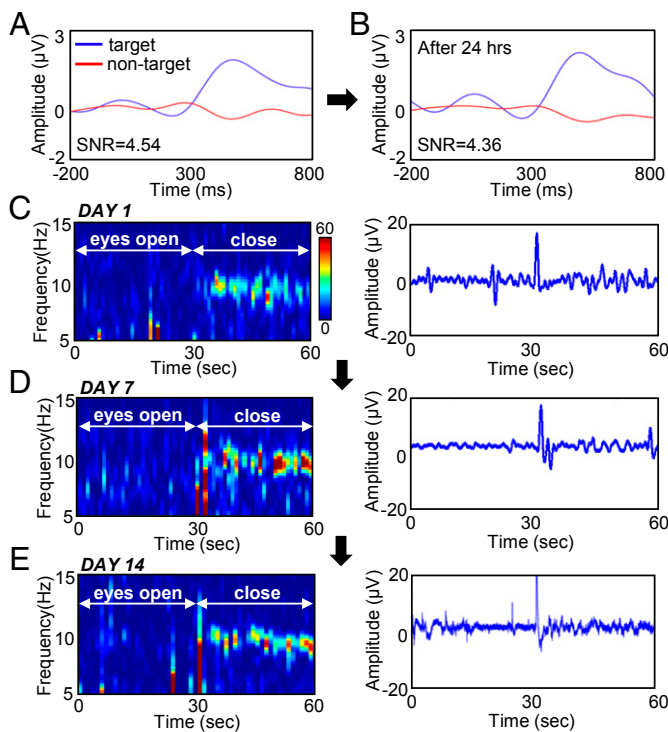


**Fig. 3.** Long-term recording of EEG. (A and B) Set of P300 data collected with an LTE electrode, immediately after mounting (A) and after 24 h (B). The SNR values are similar. (C–E) EEG alpha rhythms measured with a set of LTE electrodes for 14 d. (Left) Spectrograms showing the amplitudes as a function of the frequency for 1 min. Signals after 30 s are clearly detected when the eyes are closed. (Right) Plots presenting raw EEG signals. The data show no significant differences in signal amplitudes or patterns during 2 wk of continuous wear.

using freshly applied conventional electrodes with conductive gels (*SI Appendix*, Fig. S14).

Another example of long-term use involves recording of EEG alpha rhythms from the auricle and mastoid over a 2-wk period. Alpha rhythms typically have frequencies between 8 and 12 Hz, centered at  $\sim 10$  Hz (4). Recordings during wakeful relaxation with the eyes closed and open appear in Fig. 3 C–E. Frames on the left show EEG spectrograms for frequencies between 5 and 15 Hz; the graphs on the right present typical raw EEG signals. The sharp features that appear at  $\sim 30$  s correspond to signals that arise from blinking. The overall data reveal no significant differences from day 1 to day 14. The polymer overcoat (spray-on bandage) is breathable, thereby avoiding adverse side effects associated with sweating during activities involved in the long-term evaluations. The slightly increased levels of background noise, especially on day 14, may arise from the buildup of naturally exfoliated dead cells on the skin surface (28).

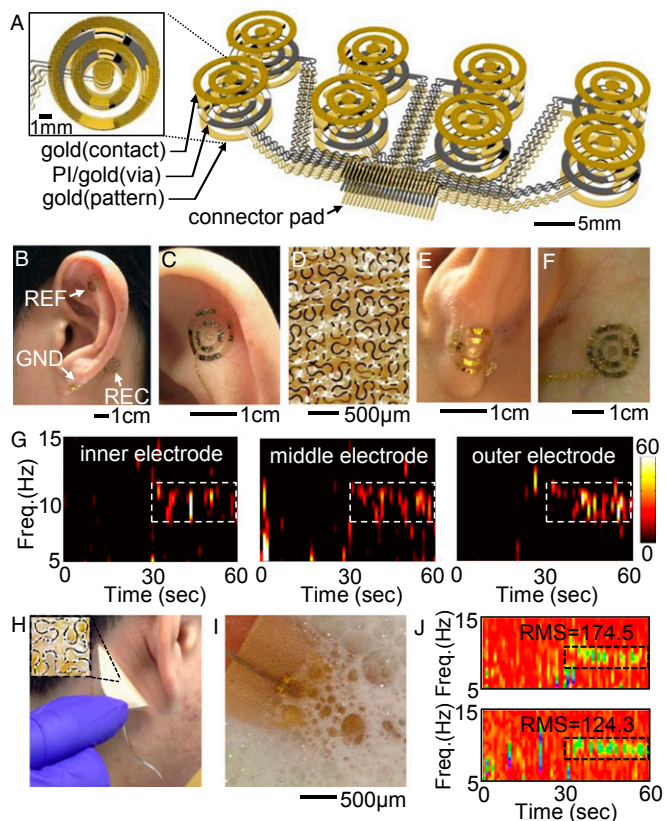
Tripolar concentric ring (TCR) and capacitive electrodes offer enhanced spatial resolution and increased levels of robustness and electrical safety in operation (Fig. 4). LTE designs afford an ability to exploit TCR layouts in ways that avoid the electrical blurring effects that occur with electrolyte gel-based systems (39). Here a single set of three ring-shaped electrodes can occupy the same area as a single, conventional electrode (1 cm in diameter) (Fig. 4A). Comparison image appears in *SI Appendix*, Fig. S15.

The 3D schematic illustration in Fig. 4A shows an array of eight epidermal TCR-LTE electrodes with top fractal electrodes (Au), interlayer dielectric (PI) and metal (Au), and a base layer of interconnects and connector pads (Au) for interfaces to external data acquisition systems (*Materials and Methods*). The

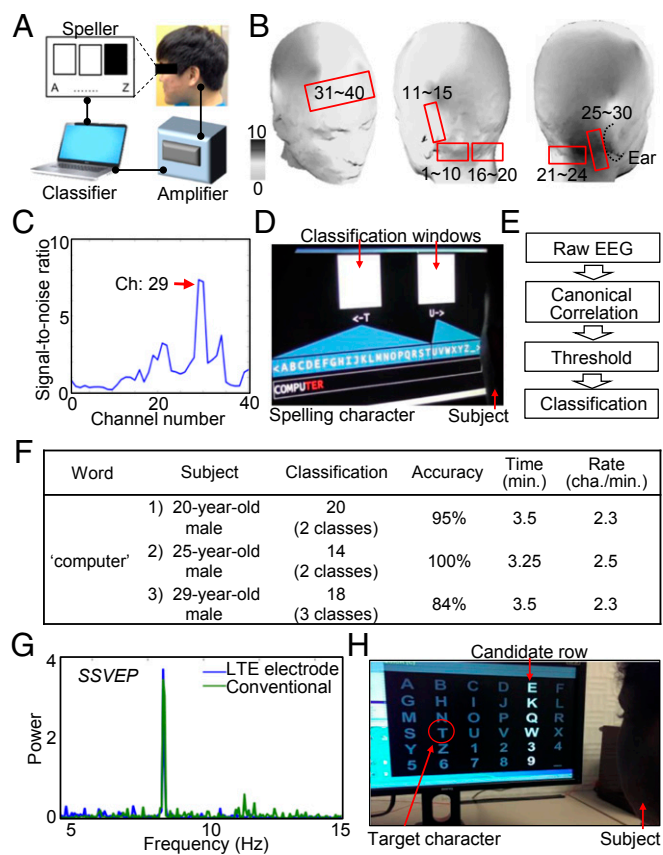
magnified illustration in Fig. 4A shows a TCR set where the top electrodes consist of fractal half-and-half patterns with a Peano design motif (*SI Appendix*, Fig. S1). Details of the fabrication steps appear in *SI Appendix*, Fig. S16 and Note S3.

Fig. 4 B–F illustrates TCR-LTE electrodes mounted on the auricle and mastoid, supported by a 3- $\mu\text{m}$ -thick elastomer. As with the basic structures of Fig. 1, each case involves conformal contact against these curvilinear surfaces. A set of TCR-LTE electrodes can readily measure EEG alpha rhythms with REC (mastoid), REF (upper antihelix), and GND (lobule) (Fig. 4B). Fig. 4 C–F presents magnified images. Fig. 4G presents spectrograms of EEG alpha rhythms from each ring electrode (inner, middle, and outer), which reveal an increased power ( $\sim 10$  Hz frequency) after the subject closed eyes (30–60 s).

Fig. 4 H–J summarizes capacitive designs using an elastomeric insulating layer (3  $\mu\text{m}$  in thickness) over the electrodes (*Materials and Methods*). This capacitive layout electrically isolates the metal components of the device from the skin (40) to avoid direct electrical loading and also to allow multiple cycles of cleaning with soap and water and disinfection with isopropyl alcohol antiseptic (25). Here the capacitive electrode (fractal Peano half-and-half) bonds to a silky, washable, silicone material (Enaltus) (Fig. 4H). For recording of EEG alpha rhythms, capacitive electrodes laminate onto the skin (mastoid and



**Fig. 4.** EEG electrodes with tripolar concentric ring (TCR) and capacitive designs. (A) Schematic illustration of TCR electrodes where a single set of three rings occupies the same area as a conventional metal electrode. (B–F) Images of TCR electrodes. (B) Integrated set of electrodes on the auricle and mastoid. (C) Enlarged view of the REF (upper antihelix). (D) Magnified view of fractal meshes. (E) GND on lobule. (F) REC on mastoid. (G) Spectrograms of EEG alpha rhythms recorded by the TCR electrodes including inner, middle, and outer rings. (H) Capacitive electrode mounted on the skin by a silky fabric. (I) Process of washing the electrode in soap water. (J) EEG alpha rhythms to compare signals before and after washing the electrode for ten cycles. The RMS values show the retained device functionality.



**Fig. 5.** Recording of steady-state visually evoked potentials (SSVEP) and P300 and their use for brain-computer interfaces. (A) Experimental setup for SSVEP-based text speller, showing a visual stimulation, a volunteer wearing electrodes, and a signal amplifier and classifier. (B) Brain mapping with 40 electrodes to identify locations that yield the highest signals. (C) Plot of SSVEP signal quality according to the location. (D) Image of the text speller interface including visual stimulation, classification algorithm, and a volunteer watching the flickering windows. (E) Flowchart of the simplified classification process. (F) Summarized performance of three subjects in the spelling task. The averaged spelling rate for “computer” with word prediction is 2.37 characters/min, and the averaged accuracy is 93%. (G) Comparison of the signals for LTE and conventional gel electrodes. Both exhibit similar patterns and amplitudes. (H) Image of the P300-based text speller to record the event-related potentials to identify the desired letter.

forehead for the REC and REF, respectively, as in *SI Appendix*, Fig. S17). Fig. 4I demonstrates the ability to wash these electrodes in soap/water. For recording, the output passes to a pre-amplifier with ultrahigh input impedance ( $> 5 \times 10^9 \Omega$  and  $\sim 110$  pF; BioRadio 150; CleveMed) to allow signal acquisition with low loss. This system provides a common-mode rejection ratio of 90 dB. Recording used 60-Hz notch and low-pass (Butterworth) filters and a sampling rate of 960 Hz, with a gain of  $\sim 50$  dB. Details appear in *SI Appendix*, Fig. S17. EEG alpha rhythms acquired before (top) and after (bottom) ten cycles of washing appear in Fig. 4J. The spectrograms clearly show alpha rhythms after 30 s with the eyes closed, with negligible differences between these cases.

The recording of EEG data and the device capabilities for continuous long-term use can be illustrated through BCI experiments. Visually evoked potentials serve as the basis for BCIs based on steady-state visually evoked potentials (SSVEP) and the P300 event-related potential. Attentional processes (41) affect the signal amplitudes, thereby rendering information on a set of user-intended targets as the basis for a BCI. Fig. 5 presents results from a BCI for a text speller. The experimental

setup in Fig. 5A includes the visual stimuli, a participant wearing the electrodes, an amplifier, an analog-to-digital converter, classifier, and software (BCI2000) (42). Three male volunteers with normal or corrected-to-normal vision demonstrate the feasibility of an SSVEP-based BCI. The experiment involved testing and experimental sessions on different days. Initial evaluations with a set of 40 conventional electrodes (Fig. 5B) yielded data to guide optimal positioning of electrodes. The numbers in Fig. 5B correspond to the channels, with a reference electrode on the ear. An optical tracking system (Polaris Vicra; NDI) identified the precise locations. Following the digitization process, each participant attended to a series of SSVEP stimuli. EEG recordings occurred during the course of 60 trials, each with a single stimulus flickering at 6, 6.67, 7.5, 8.57, or 10 Hz for 20 s, with 5 s between trials and a null condition. The algorithms to determine optimal placement and to classify the online experiments were based on canonical correlation analysis (CCA) (43). This process is visualized using a topographic map of the SNR ratio (Fig. 5B). Fig. 5C presents an alternative representation of this data according to the channels (subject 2 at a stimulation frequency of 8.57 Hz).

Fig. 5D illustrates the text speller interface, which includes a question posed to the user, defined as a mapping from the visual targets to a set of possible characters. The highlighted characters in Fig. 5D illustrate such a mapping. Each visual target flickers at a unique frequency, allowing a CCA-based classifier to determine the user's desired character. The simplified classification steps appear in the flowchart of Fig. 5E. When the user chooses a target, the interface updates a model of its belief and then selects a new query. Three subjects attempted to spell “computer” with the assistance of word prediction algorithms (44). Fig. 5F summarizes the performance for three subjects (*SI Appendix*, Movie S1, from subject 2). The averaged spelling rate is 2.37 characters per min, which is only a factor of two to three times slower than a full cap system that uses 8–10 electrodes on the hairy scalp (4–7 characters per min) (45). Fig. 5G compares an SSVEP from an LTE electrode with that from a conventional electrode (subject 2, channel 23). The results exhibit similar patterns and amplitudes.

P300 event-related potentials (ERP) provide an additional example of a BCI (Fig. 5H). This study began with acquisition of baseline data using conventional electrodes at four sites (each auricle, mastoid, and forehead) and compared with LTE electrodes to measure P300 ERP. A participant responded to a series of words including “brown,” “fox,” “epidermal,” and “electrode.” Our data primarily show components of the P300 at 0.3–4 Hz. The data were baseline corrected to the 200-ms period before the stimulus onset and then averaged to yield an ERP. The result of the recorded P300 ERP (Fig. 3A and B) clearly distinguishes responses to target and nontarget stimuli.

The collection of results presented here illustrates that extremely compliant electrodes allow integration with demanding regions of the head such as the auricle, for long-term EEG recording, without gels, via direct contact or capacitive coupling. The system level fractal design for both the electrodes and the interconnects is a critical feature that affords excellent levels of both bendability ( $>180^\circ$ ) and stretchability ( $>50\%$ ). Thermal imaging and EEG studies provide evidence for noninvasive, biocompatible interfaces to the skin, with electrical properties that support invariant recording quality over periods that extend to 2 wk. Areas for future work include further modeling and experimental study of tripolar electrodes and development of wireless communication and power supply systems that can integrate with these auricle mounted electrodes.

## Materials and Methods

**Fabrication of Epidermal Electrodes.** The device preparation used conventional microfabrication techniques (details in *SI Appendix*, Note 1 and Figs. S2–S5). A silicon wafer served as a support for a sacrificial layer of polymethyl

methacrylate (100 nm in thickness) and an overcoat of polyimide (1.2  $\mu\text{m}$  in thickness). Metal evaporation, photolithography, and etching defined fractal layouts. A water-soluble tape (3M) allowed retrieval of these structures after dissolution of the sacrificial layer, thereby enabling transfer onto a silicone elastomer (3  $\mu\text{m}$  in thickness), supported by a water dissolvable polymer sheet.

**Fabrication of Tripolar Electrodes.** The fabrication of tripolar electrodes involved formation of multiple layers of Au-PI (via)-Au using standard micro-fabrication techniques (details in *SI Appendix, Note 2 and Fig. S16*). An additional step of metal evaporation yielded a 500-nm-thick layer of Au for connection with the prepatterned Au through the PI layer. Patterning, retrieval, and transfer of fractal traces followed the same methods used for fabrication of epidermal electrodes, described above.

**Fabrication of Capacitive Electrodes.** The processing for capacitive devices included spin coating of a dielectric layer (3- $\mu\text{m}$ -thick elastomer) on Au electrodes. This layer protected the electrodes and allowed only capacitive coupling to the skin, thereby ensuring electrically safe, robust recording of EEG. Such structures are also reusable and compatible with cleaning using soap and water.

**Calculation of the Signal-to-Noise Ratio.** This calculation used the Welch periodogram in MatLab (Mathworks) across the bandwidth of 5–30 Hz. Averaging the periodograms calculated for each trial yielded a single power

spectrum. The power of the noise signal corresponds to the average value of those bins in the frequency domain outside of the range of the frequency of the signal ( $\pm 0.3$  Hz) or any of its harmonics. The power of the signal corresponds to the sum of the maximum power in the frequency range of the signal and its first two harmonics minus the average power of the bins at the frequency of stimulation. EEGLAB (function: topoplot) (46) plotted the SNR values as a topographical map.

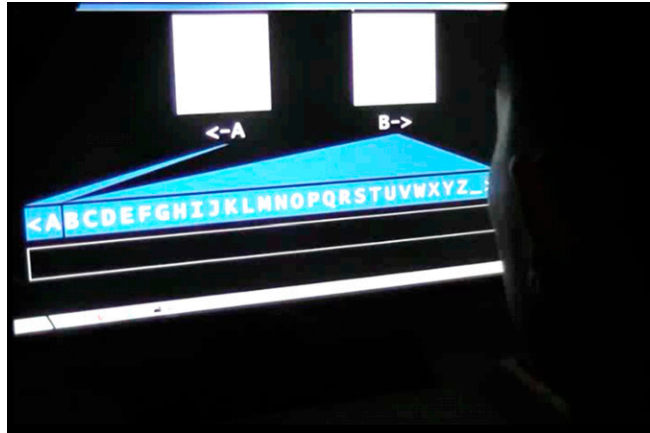
**Experiments on Human Subjects.** The experiments for recording of EEG alpha rhythms and thermal imaging with TCR and capacitive electrodes involved three volunteers and were all performed at Virginia Commonwealth University [institutional review board (IRB) approved protocol: HM20001454]. The experiments for SSVEP and P300 recording were conducted at the University of Illinois at Urbana-Champaign (IRB approved protocol: 13453).

**ACKNOWLEDGMENTS.** The materials aspects of the work were supported by the US Department of Energy, Office of Science, Basic Energy Sciences, under Award DE-FG02-07ER46741. W.-H.Y. acknowledges startup funding from the School of Engineering and research development support from Center for Rehabilitation Science and Engineering, Virginia Commonwealth University. J.J.S.N. acknowledges support from the Integrative Graduate Education and Research Traineeship, Neuroengineering program at the University of Illinois at Urbana-Champaign. J.W.L. and U.P. thank the Global Research Laboratory Program (K20704000003TA050000310) through the National Research Foundation, the Ministry of Science, Korea. H.C. is a Howard Hughes Medical Institute International Student Research fellow.

- Haas LF (2003) Hans Berger (1873-1941), Richard Caton (1842-1926), and electroencephalography. *J Neurol Neurosurg Psychiatry* 74(1):9.
- Smith SJM (2005) EEG in the diagnosis, classification, and management of patients with epilepsy. *J Neurol Neurosurg Psychiatry* 76(Suppl 2):ii2-ii7.
- Kutas M, Federmeier KD (2000) Electrophysiology reveals semantic memory use in language comprehension. *Trends Cogn Sci* 4(12):463-470.
- Babiloni C, et al. (2014) Cortical EEG alpha rhythms reflect task-specific somatosensory and motor interactions in humans. *Clin Neurophysiol* 125(10):1936-1945.
- Searle A, Kirkup L (2000) A direct comparison of wet, dry and insulating bioelectric recording electrodes. *Physiol Meas* 21(2):271-283.
- Ferree TC, Luu P, Russell GS, Tucker DM (2001) Scalp electrode impedance, infection risk, and EEG data quality. *Clin Neurophysiol* 112(3):536-544.
- David Hairston W, et al. (2014) Usability of four commercially-oriented EEG systems. *J Neural Eng* 11(4):046018.
- Lopez-Gordo MA, Sanchez-Morillo D, Pelayo Valle F (2014) Dry EEG electrodes. *Sensors (Basel)* 14(7):12847-12870.
- Salvo P, et al. (2012) A 3D printed dry electrode for ECG/EEG recording. *Sens Actuators A Phys* 174:96-102.
- Grozea C, Voinescu CD, Fazli S (2011) BCI-sensors—Low-cost flexible passive dry EEG electrodes for neurofeedback and BCI applications. *J Neural Eng* 8(2):025008.
- Liao LD, Wang JJ, Chen SF, Chang JY, Lin CT (2011) Design, fabrication and experimental validation of a novel dry-contact sensor for measuring electroencephalography signals without skin preparation. *Sensors (Basel)* 11(6):5819-5834.
- Chi YM, Jung TP, Cauwenberghs G (2010) Dry-contact and noncontact biopotential electrodes: Methodological review. *IEEE Rev Biomed Eng* 3:106-119.
- Oehler M, Neumann P, Becker M, Curio G, Schilling M (2008) Extraction of SSVEP signals of a capacitive EEG helmet for human machine interface. *Conf Proc IEEE Eng Med Biol Soc* 2008:4495-4498.
- Lee SM, et al. (2014) Self-adhesive epidermal carbon nanotube electronics for tether-free long-term continuous recording of biosignals. *Sci Rep* 4:6074.
- Mota AR, et al. (2013) Development of a quasi-dry electrode for EEG recording. *Sens Actuators A Phys* 199:310-317.
- Myers AC, Huang H, Zhu Y (2015) Wearable silver nanowire dry electrodes for electrophysiological sensing. *RSC Adv* 5(15):11627-11632.
- Bundy D, Leuthardt E (2014) *An Ipsilateral, Contralesional BCI in Chronic Stroke Patients. Brain-Computer Interface Research*, SpringerBriefs in Electrical and Computer Engineering, eds Guger C, Vaughan T, Allison B (Springer, New York), pp 19-29.
- Marlow N, Wolke D, Bracewell MA, Samara M; EPICure Study Group (2005) Neurological and developmental disability at six years of age after extremely preterm birth. *N Engl J Med* 352(1):9-19.
- Wang LF, Liu JQ, Yang B, Yang CS (2012) PDMS-based low cost flexible dry electrode for long-term EEG measurement. *IEEE Sens J* 12(9):2898-2904.
- Wang L-F, Liu J-Q, Yan X-X, Yang B, Yang C-S (2013) A MEMS-based pyramid micro-needle electrode for long-term EEG measurement. *Microsyst Technol* 19(2):269-276.
- Lee SM, et al. (2013) A capacitive, biocompatible and adhesive electrode for long-term and cap-free monitoring of EEG signals. *J Neural Eng* 10(3):036006.
- Hoon Lee J, et al. (2014) CNT/PDMS-based canal-typed ear electrodes for inconspicuous EEG recording. *J Neural Eng* 11(4):046014.
- Costa JC, Da-Silva PJ, Almeida RM, Infantosi AF (2014) Validation in principal components analysis applied to EEG data. *Comput Math Methods Med* 2014:413801.
- Looney D, et al. (2012) The in-the-ear recording concept: User-centered and wearable brain monitoring. *IEEE Pulse* 3(6):32-42.
- Hattori Y, et al. (2014) Multifunctional skin-like electronics for quantitative, clinical monitoring of cutaneous wound healing. *Adv Healthc Mater* 3(10):1597-1607.
- Kim DH, et al. (2011) Epidermal electronics. *Science* 333(6044):838-843.
- Jeong JW, et al. (2013) Materials and optimized designs for human-machine interfaces via epidermal electronics. *Adv Mater* 25(47):6839-6846.
- Yeo W-H, et al. (2013) Multifunctional epidermal electronics printed directly onto the skin. *Adv Mater* 25(20):2773-2778.
- Giselbrecht S, Rapp BE, Niemeyer CM (2013) The chemistry of cyborgs—Interfacing technical devices with organisms. *Angew Chem Int Ed Engl* 52(52):13942-13957.
- Hammock ML, Chortos A, Tee BCK, Tok JBH, Bao Z (2013) 25th anniversary article: The evolution of electronic skin (e-skin): A brief history, design considerations, and recent progress. *Adv Mater* 25(42):5997-6038.
- Ningqi L, Jun D, Ni Z, Leung BHK, Poon CCY (2014) Mobile health: Design of flexible and stretchable electrophysiological sensors for wearable healthcare systems. *2014 11th International Conference on Wearable and Implantable Body Sensor Networks (BSN)* (IEEE Computer Society Washington, DC), pp 87-91.
- Pang C, et al. (2015) Highly skin-conformal microhair sensor for pulse signal amplification. *Adv Mater* 27(4):634-640.
- Voskerician G, et al. (2003) Biocompatibility and biofouling of MEMS drug delivery devices. *Biomaterials* 24(11):1959-1967.
- Baek D-H, et al. (2014) A thin film polyimide mesh microelectrode for chronic epidural electrocorticography recording with enhanced contactability. *J Neural Eng* 11(4):046023.
- Dencheva M, et al. (2014) Thermovision in dental allergology. *J IMAB* 20(3):558-562.
- Padilla-Medina JA, et al. (2014) Assessment technique for acne treatments based on statistical parameters of skin thermal images. *J Biomed Opt* 19(4):046019.
- Liao LD, et al. (2012) Gaming control using a wearable and wireless EEG-based brain-computer interface device with novel dry foam-based sensors. *J Neuroeng Rehabil* 9:5.
- Lin CT, et al. (2011) Novel dry polymer foam electrodes for long-term EEG measurement. *IEEE Trans Bio-Med Eng* 58(5):1200-1207.
- Prats-Boluda G, Ye-Lin Y, Garcia-Breijo E, Ibanez J, Garcia-Casado J (2012) Active flexible concentric ring electrode for non-invasive surface bioelectrical recordings. *Meas Sci Technol* 23(12):125703.
- Jeong JW, et al. (2014) Capacitive epidermal electronics for electrically safe, long-term electrophysiological measurements. *Adv Healthc Mater* 3(5):642-648.
- Müller MM, Hillyard S (2000) Concurrent recording of steady-state and transient event-related potentials as indices of visual-spatial selective attention. *Clin Neurophysiol* 111(9):1544-1552.
- Schalk G, McFarland DJ, Hinterberger T, Birbaumer N, Wolpaw JR (2004) BCI2000: A general-purpose, brain-computer interface (BCI) system. *IEEE Trans Bio-Med Eng* 51(6):1034-1043.
- Bin G, Gao X, Yan Z, Hong B, Gao S (2009) An online multi-channel SSVEP-based brain-computer interface using a canonical correlation analysis method. *J Neural Eng* 6(4):046002.
- Akce A (2013) Human control of robots over discrete noisy channels with high latency: Toward efficient EEG-based brain-robot interfaces. Doctoral dissertation (University of Illinois at Urbana-Champaign, Champaign, IL).
- Cecotti H (2010) A self-paced and calibration-less SSVEP-based brain-computer interface speller. *IEEE Trans Neural Syst Rehabil Eng* 18(2):127-133.
- Delorme A, Makeig S (2004) EEGLAB: An open source toolbox for analysis of single-trial EEG dynamics including independent component analysis. *J Neurosci Methods* 134(1):9-21.

# Supporting Information

Norton et al. 10.1073/pnas.1424875112



Movie S1. Steady-state visually evoked potential-based text spelling of "computer."

[Movie S1](#)

## Other Supporting Information Files

[SI Appendix \(PDF\)](#)

**Supporting Information for:**

**Soft, curved electrode systems capable of integration on the auricle as a persistent brain-computer interface**

James J. S. Norton<sup>a</sup>, Dong Sup Lee<sup>b,c</sup>, Jung Woo Lee<sup>d,e</sup>, Woosik Lee<sup>e</sup>, Ohjin Kwon<sup>c</sup>, Phillip Won<sup>d</sup>, Sung-Young Jung<sup>d,f</sup>, Huanyu Cheng<sup>g</sup>, Jae-Woong Jeong<sup>h</sup>, Abdullah Akce<sup>i</sup>, Stephen Umunna<sup>j</sup>, Ilyoun Na<sup>d,k</sup>, Yong Ho Kwon<sup>d</sup>, Xiaoqi Wang<sup>l</sup>, Zhuangjian Liu<sup>m</sup>, Ungyu Paik<sup>e</sup>, Yonggang Huang<sup>g</sup>, Timothy Bretl<sup>n</sup>, Woon-Hong Yeo<sup>c,1</sup>, and John A. Rogers<sup>d,1</sup>

<sup>a</sup>Neuroscience Program, University of Illinois at Urbana-Champaign Urbana, IL 61801

<sup>b</sup>Department of Chemical and Life Science Engineering, Virginia Commonwealth University, Richmond, VA 23284

<sup>c</sup>Department of Mechanical and Nuclear Engineering, Center for Rehabilitation Science and Engineering, Virginia Commonwealth University, Richmond, VA 23284

<sup>d</sup>Department of Materials Science and Engineering, University of Illinois at Urbana-Champaign, Urbana, IL 61801

<sup>e</sup>Department of Materials Science and Engineering, Department of Energy Engineering, Hanyang University, Seoul 133-791, Republic of Korea

<sup>f</sup>Department of Mechanical Engineering, Pohang University of Science and Technology, Pohang, 790-784, Republic of Korea

<sup>g</sup>Departments of Civil and Environmental Engineering and Mechanical Engineering, Center for Engineering and Health, Skin Disease Research Center, Northwestern University, Evanston, IL 60208

<sup>h</sup>Department of Electrical, Computer, and Energy Engineering, University of Colorado, Boulder, CO 80309

<sup>i</sup>Google Inc., Mountain View, CA 94043

<sup>j</sup>Department of Molecular and Integrative Physiology, University of Illinois at Urbana-Champaign, Urbana, IL 61801

<sup>k</sup>Department of Chemical Engineering, Pohang University of Science and Technology, Pohang, 790-784,  
Republic of Korea

<sup>l</sup>Department of Dermatology, Feinberg School of Medicine, Northwestern University, Chicago, IL 60611

<sup>m</sup>Institute of High Performance Computing, 1 Fusionopolis Way, #16-16 Connexis North 138632,  
Singapore

<sup>n</sup>Department of Aerospace Engineering, University of Illinois at Urbana-Champaign, Urbana, IL 61801

**<sup>1</sup>Corresponding author:**

Prof. Woon-Hong Yeo, 401 W Main St, Richmond, VA 23233, 804-827-3517, whyeo@vcu.edu

Prof. John A. Rogers, 104 S Goodwin Ave, Urbana, IL 61801, 217-333-1370, jrogers@illinois.edu

### **Supporting Note 1.**

Fabrication process of epidermal electrodes follows exploits modified versions of otherwise conventional microfabrication techniques, together with processes of transfer printing.

#### a) Preparing of a carrier wafer

1. Clean a silicon wafer with acetone, IPA, and DI water.
2. Dehydrate it on a hot plate at 110 °C for 3 min.
3. Expose UV onto the wafer to make the surface hydrophilic for 3 min.
4. Spincoat PMMA on the wafer at 2000 rpm for 30 seconds.
5. Cure it on a hot plate at 180 °C for 2 minutes 30 seconds.

#### b) Material deposition and photolithography

1. Spincoat polyimide at 4000 rpm for 1 min.
2. Pre-bake it on a hot plate at 150 °C for 5 min.
3. Hard bake it in a hot oven at 250 °C for 2 hours.
4. Deposit 5nm/200nm-thick chromium/gold (Cr/Au) using an electron beam evaporator
5. Spincoat photoresist (AZ 5214) at 3000 rpm for 30 seconds.
6. Cure it on a hot plate at 110 °C for 1min.
7. Align(Metal#1) and expose UV (fractal and FS interconnect patterns).
8. Develop it with a base developer (917MIF).
9. Etch Cr/Au using chromium and gold etchant
10. Remove photoresist using acetone.
11. Spincoat 2nd layer of polyimide at 4000 rpm for 1 min.
12. Pre-bake it on a hot plate at 150 °C for 5 min.

13. Hard bake it in a hot oven at 250 °C for 2 hours.
14. Spincoat photoresist (AZ 4620) at 900/1100/4000 rpm for 10/60/20 seconds.
15. Cure it on a hot plate at 75 °C for 30 min.

c-1) Patterning of interconnects. Interconnects (non-sensing area) will have Au layer covered by polyimide layer.

1. Align(PI#2) and expose UV (encapsulation patterns on the pre-patterns). Develop it with a 1:2 mixture of base developer (400k) and deionized (DI) water. Photoresist remains in the connector pattern to protect etching of polyimide layer.
2. Etch the patterned two layers of polyimides using reactive ion etcher (RIE, March) at 150 W, 170 mTorr, 20 sccm oxygen for 1500 seconds.
1. Remove photoresist using acetone.

c-2) Patterning of sensors and contact pads. Sensors and contact pads will have Au surface exposed. Therefore, upon aligning and developing, PR will be removed.

1. Align(PI#2) and expose UV (encapsulation patterns on the pre-patterns). Develop it with a 1:2 mixture of base developer (400k) and deionized (DI) water. Photoresist layer in the sensors and contact pads is developed completely in order to etch the polyimide layer to expose patterned Au surface of the sensors and contact pads.
2. Etch the patterned two layers of polyimides using reactive ion etcher (RIE, March) at 150 W, 170 mTorr, 20 sccm oxygen for 1500 seconds.
3. Remove photoresist using acetone.

d-1) Preparation of a thick elastomeric membrane

1. Prepare a petri dish to hold silicone material
2. Mix part B, add part A, and mix together thoroughly (Solaris, Smooth-On). Spincoat the mixture in petri dish at 300 rpm for 1 min, which offers ~500  $\mu\text{m}$ -thick substrate. Cure it at room temperature.
3. Gently detach silicone from the petri dish.

d-2) Preparation of a thin elastomeric membrane on PVA (polyvinyl alcohol; Haining Sprutop Chemical Tech, China).

1. Tape PVA onto a glass.
2. Prepare 2:1 Ecoflex (part B is 2) and spincoat at 3000rpm for 120s.
3. Cure it in a oven at 75 °C for 1 hour.

e-1) Pick up and transfer printing of electronics onto a thick membrane

1. Deposit  $\text{SiO}_2$  (50 nm) using an electron beam evaporator.
2. Expose UV onto the targeted silicone for 3 min.
3. Transfer the patterns on the silicone substrate.
4. Dissolve the tape by putting them in water for 1 hours.
5. Bonding flexible electrical cable.

e-2) Pick up and transfer printing of electronics onto a thin membrane/PVA

1. Deposit  $\text{SiO}_2$  (50 nm) using an electron beam evaporator.
2. Expose UV onto the targeted silicone/PVA substrate for 3 min.
3. Transfer the patterns on the silicone/PVA substrate.

4. Dissolve the tape by gently applying water on the water soluble tape only, applying water onto silicone/PVA substrate will dissolve PVA.

5. Bonding flexible electrical cable.

## Supporting Note 2

Fabrication process of tri-polar electrodes follows exploits modified versions of otherwise conventional microfabrication techniques, together with processes of transfer printing.

1. Tri-polar fabrication continues after following all the steps in Supporting Note 1b.
2. Align(PI#2) and expose UV (encapsulation patterns on the pre-patterns). Develop it with a 1:2 mixture of base developer (400k) and deionized (DI) water.
3. Etch the patterned one layer(via) of polyimides using reactive ion etcher (RIE, March) at 150 W, 170 mTorr, 20 sccm oxygen for 600 seconds.
4. Remove photoresist using acetone
5. Deposit 500nm-thick Au using electron beam evaporator.
6. Spincoat photoresist (AZ 5214) at 3000 rpm for 30 seconds.
7. Cure it on a hot plate at 110 °C for 1min.
8. Align(Metal via#3) and expose UV (fractal and FS interconnect patterns). Develop it with a base developer (917MIF).
9. Etch Au using gold etchant.
10. Remove photoresist using acetone.
11. Spincoat photoresist (AZ 4620) at 900/1100/4000 rpm for 10/60/20 seconds.
12. Cure it on a hot plate at 75 °C for 30 min.
13. Align(PI#4) and expose UV. Develop it with a 1:2 mixture of base developer (400k) and deionized (DI) water.
14. Etch the patterned one layer of polyimides using reactive ion etcher (RIE, March) at 150 W, 170 mTorr, 20 sccm oxygen for 600 seconds.
15. Remove photoresist using acetone.

## Supporting Figure Legends

**Fig. S1.** Fractal patterns based on 'Peano' curves that include arc sections to avoid stress concentrations at the corners. There are 2<sup>nd</sup> order iteration of Peano curves to form 'half-and-half' and 'all vertical' shapes.

**Fig. S2.** Fabrication process of epidermal electrodes: A) preparing a carrier wafer.

**Fig. S3.** Fabrication process of epidermal electrodes: B) material deposition and photolithography

**Fig. S4.** Fabrication process of epidermal electrodes: C-1) patterning of interconnects, C-2) patterning of sensors and contact pads, D-1) preparation of a thick elastomeric membrane, and D-2) preparation of a thin elastomeric membrane on PVA.

**Fig. S5.** Fabrication process of epidermal electrodes: E-1) pick up and transfer printing of electronics onto a thick membrane, E-2) pick up and transfer printing of electronics onto a thin membrane/PVA.

**Fig. S6.** Comparison of EEG alpha rhythms (spectrograms). (A) Noisy signals caused by incomplete mounting of the device. (B) Clear signals from the device with intimate contact to the skin.

**Fig. S7.** Results of finite element method for analysis of the epidermal device (electrode and interconnects) under uniaxial tensile loads. Scale bars show the maximum principal strains for fractal (metal) and substrate (silicone elastomer), respectively.

**Fig. S8.** Image of motion of the knee joint with the skin-mounted stretchable bandage that demonstrates the maximum deformation of ~50 % in length.

**Fig. S9.** EEG alpha rhythms recorded by epidermal electrodes mounted on the auricle and mastoid: spectrogram on the left shows the amplitudes of alpha rhythms when eyes were closed and plot on the right presents raw EEG signals as a function of the frequency.

**Fig. S10.** Images of electrolyte gel on a conventional electrode that shows a ~50 % reduction in volume due to evaporative drying over 6 hours.

**Fig. S10.** (A – B) Schematic illustrations that present the experimental setup including a skin replica (elastomer), gel electrode, mounting tape, and a hot plate: top view (A) and cross-sectional view (B). (C) Images of electrolyte gel on a conventional electrode that shows a ~50 % reduction in volume due to evaporative drying over 6 hours.

**Fig. S11.** (A) Image of a LTE electrode (inset: magnified view of the contact pads). (B) Image of a mounted LTE electrode on mastoid. (C) Image of positioning of the connector to the electrode by using a tweezer.

**Fig. S12.** (A) Schematics of the design of a releasable connector. (B) Image of the fabricated connector on a silicone elastomer that is integrated with anisotropic conductive films.

**Fig. S13.** Qualitative monitoring of the skin by a USB digital microscope (left) and the image of the skin (right).

**Fig. S14.** (A) Recording of P300 signals using a conventional electrode. (B) P300 data collected with the conventional electrode.

**Fig. S15.** Comparison of the size of electrodes between the conventional electrode and tripolar concentric ring electrode.

**Fig. S16.** Details of microfabrication steps for tripolar concentric ring electrodes.

**Fig. S17.** (A) Schematic diagrams of electrical circuits of the capacitive epidermal electrodes mounted on the skin. (B) Plot of pre-amplifier gain as a function of frequency.

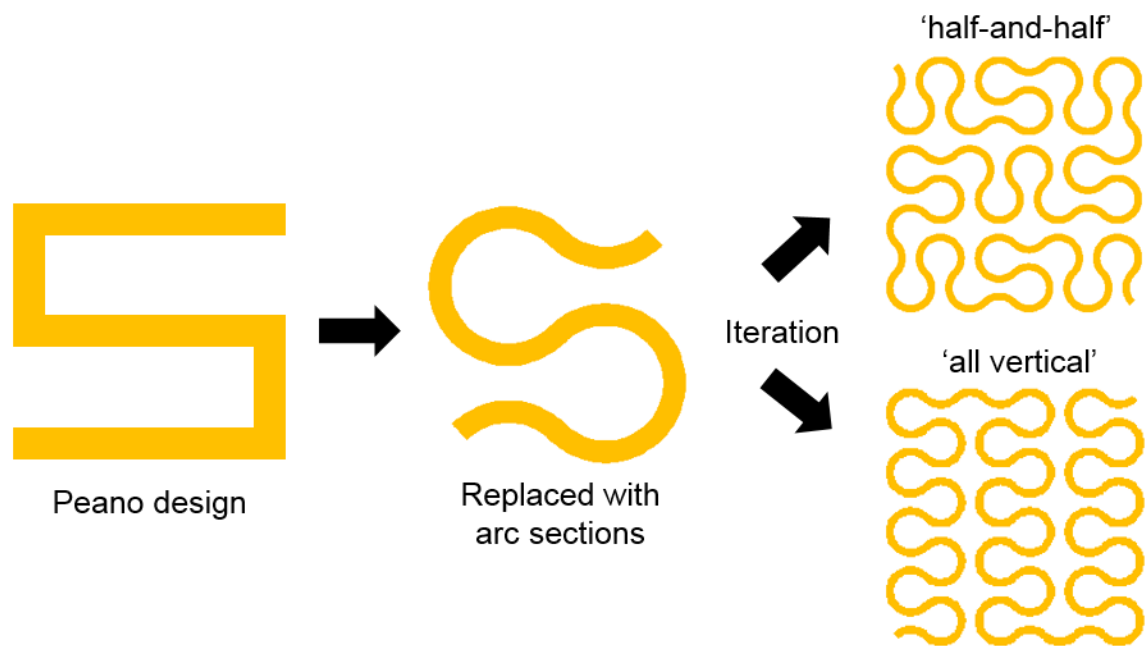


**Figure S1**

### A) Preparing of a carrier wafer

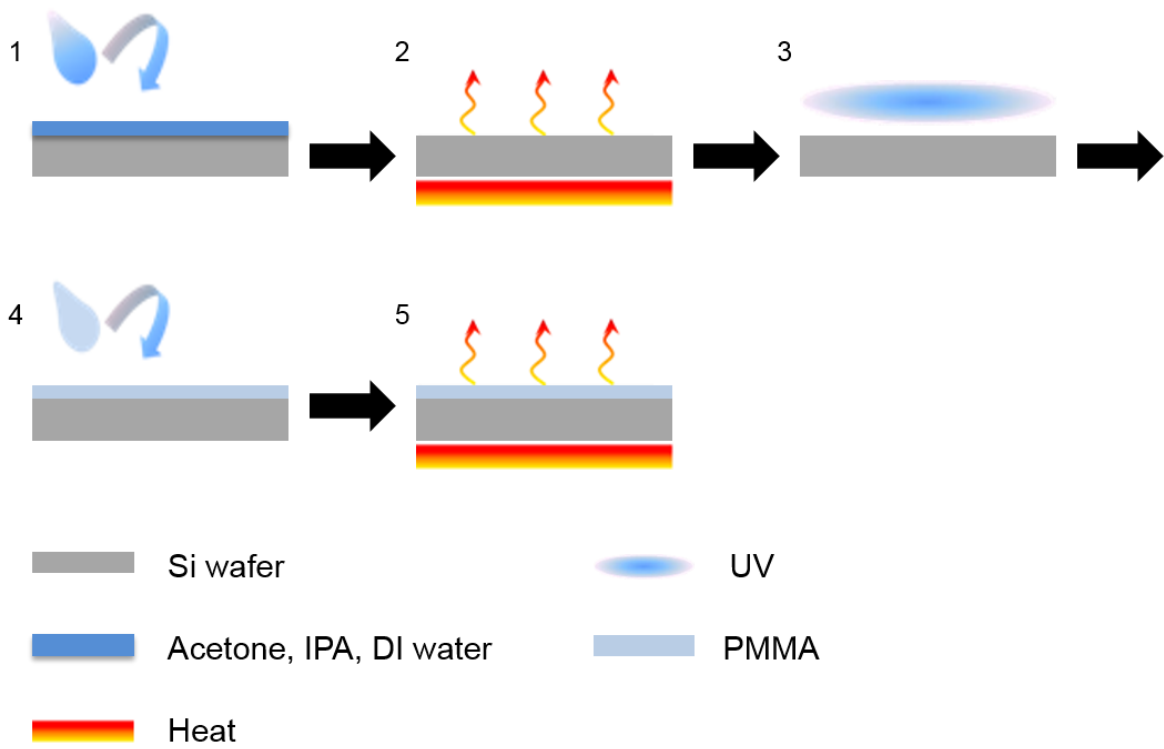


Figure S2

### B) Material deposition and photolithography

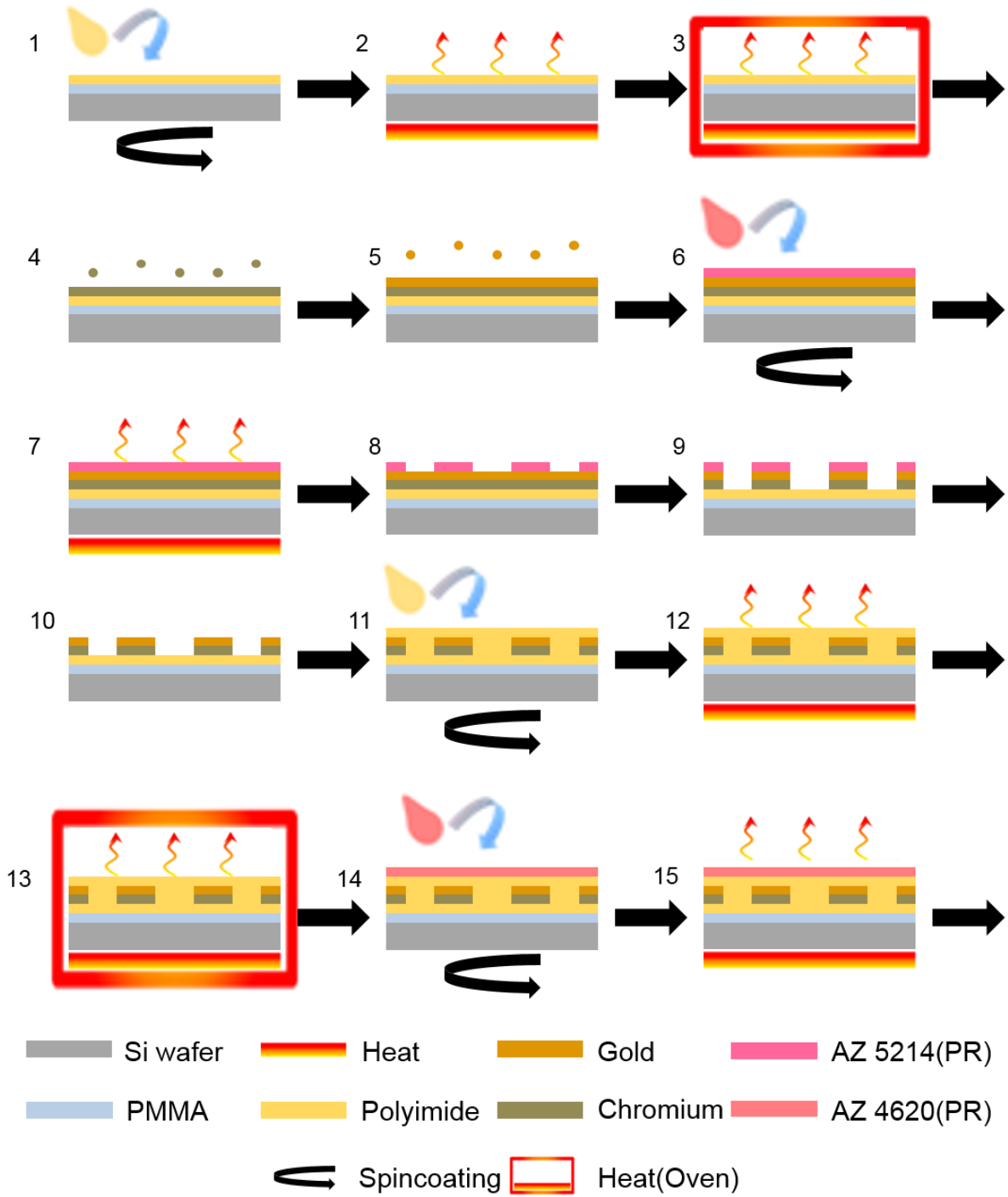
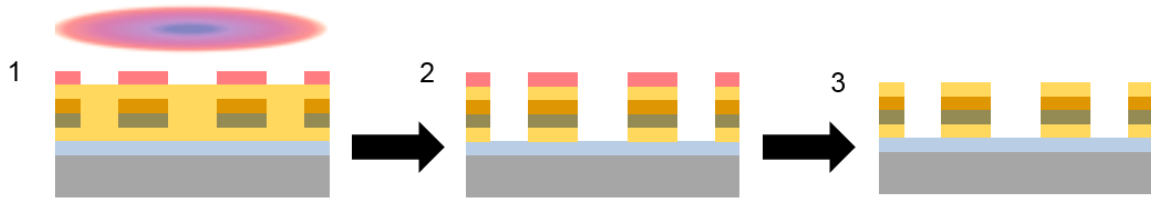
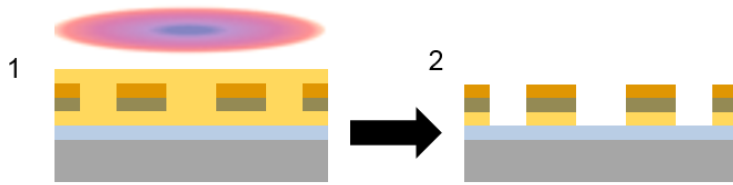


Figure S3

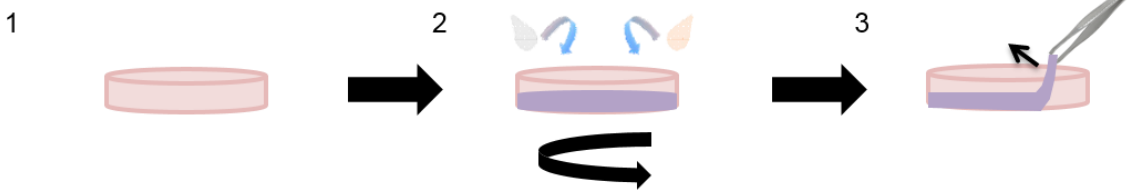
### C-1) Patterning of interconnects



### C-2) Patterning of sensors and contact pads



### D-1) Preparation of a thick elastomeric membrane



### D-2) Preparation of a thin elastomeric membrane on PVA

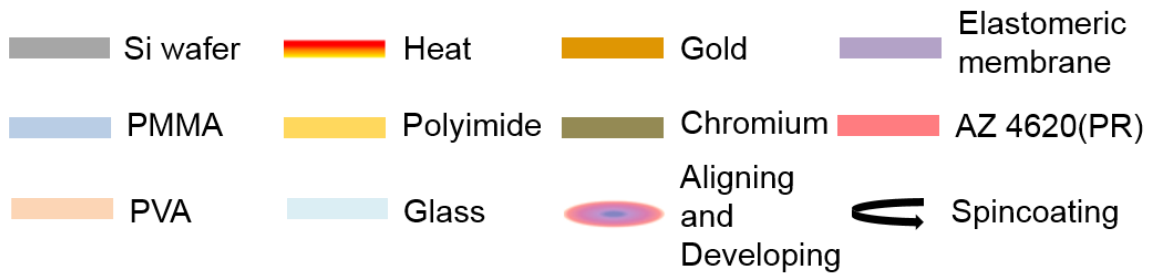
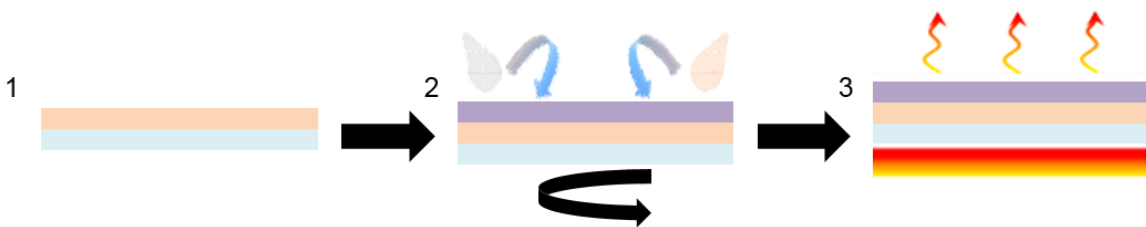
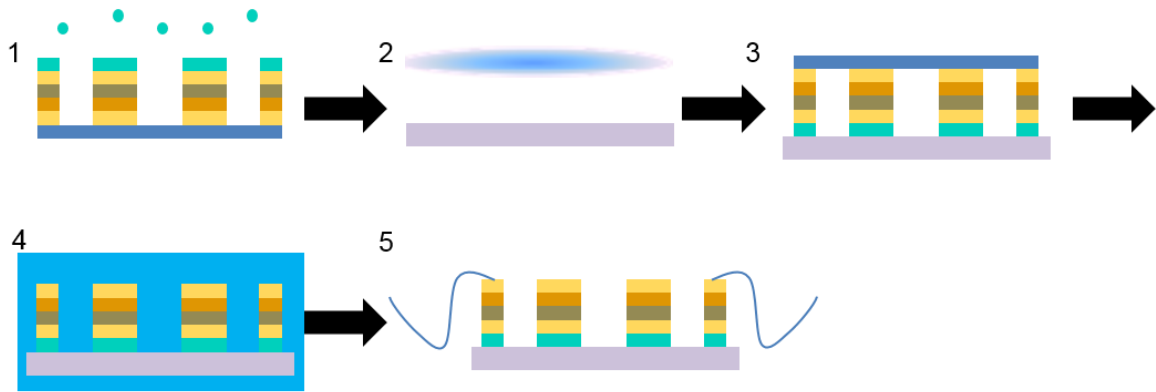
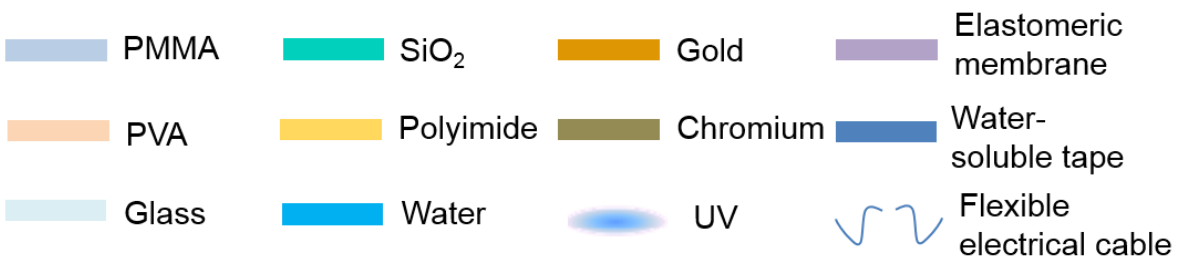
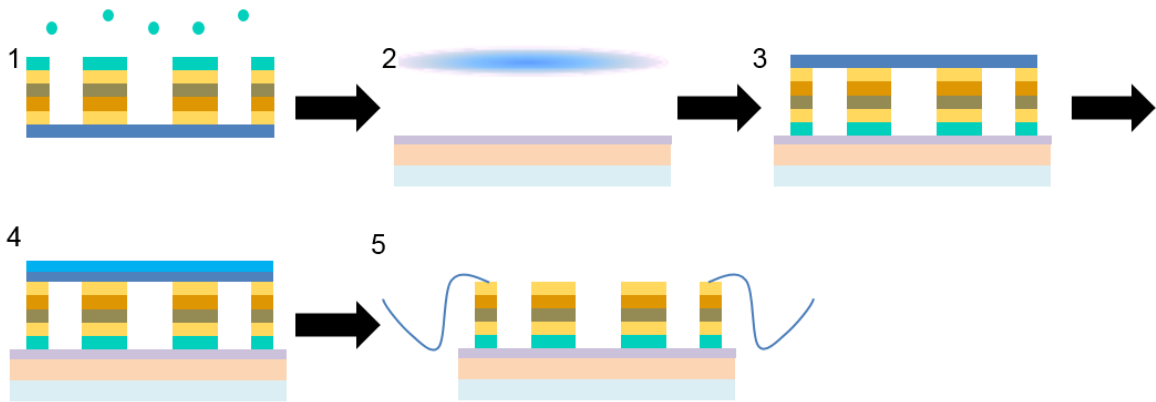


Figure S4

**E-1) Pick up and transfer printing of electronics onto a thick membrane**



**E-2) Pick up and transfer printing of electronics onto a thin membrane/PVA**



**Figure S5**

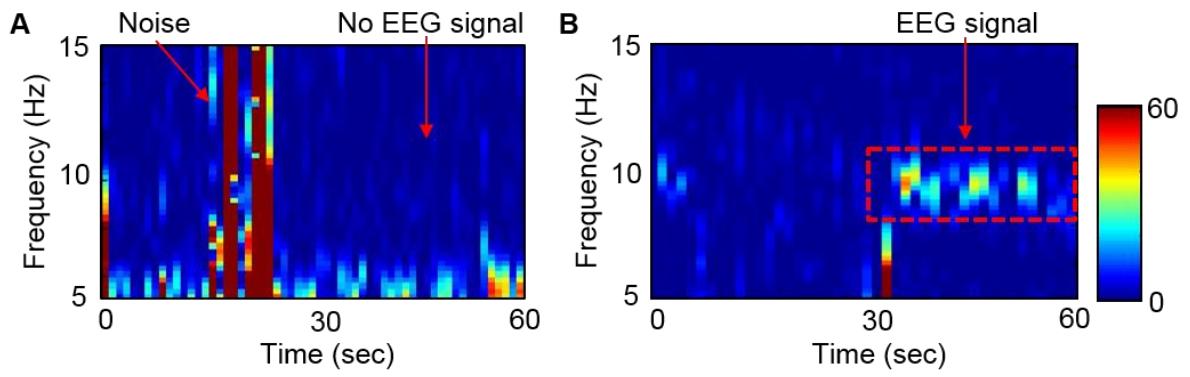


**Figure S6**

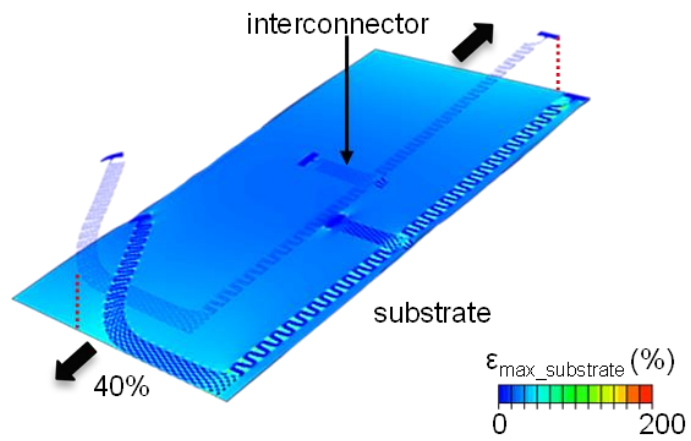
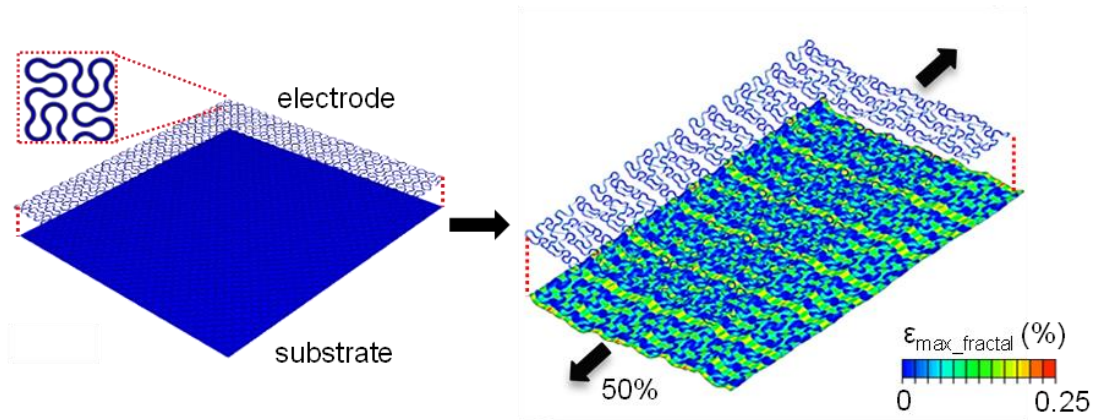
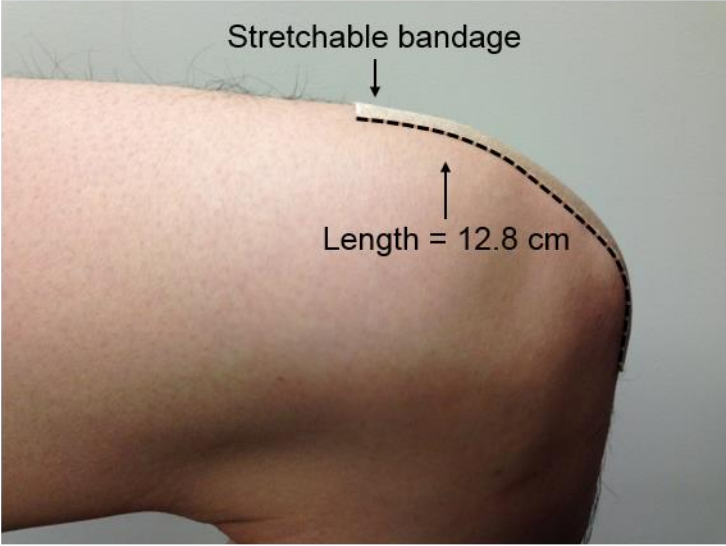
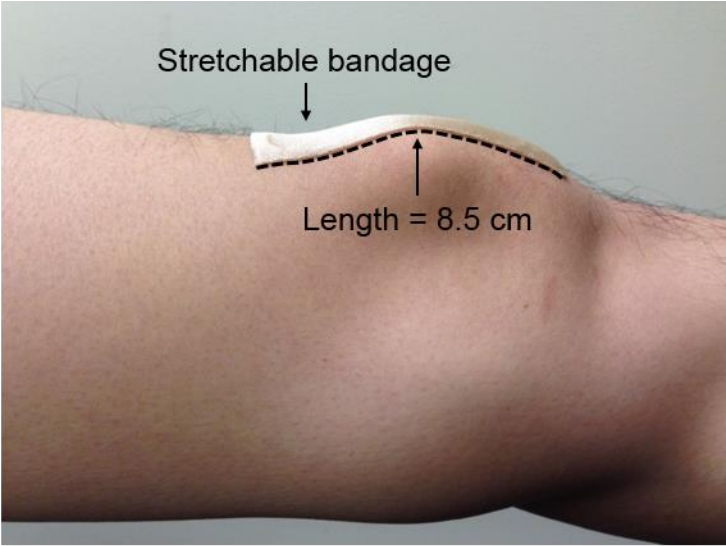


Figure S7



2 cm

A horizontal black scale bar representing 2 cm, located at the bottom right of the lower photograph.

**Figure S8**

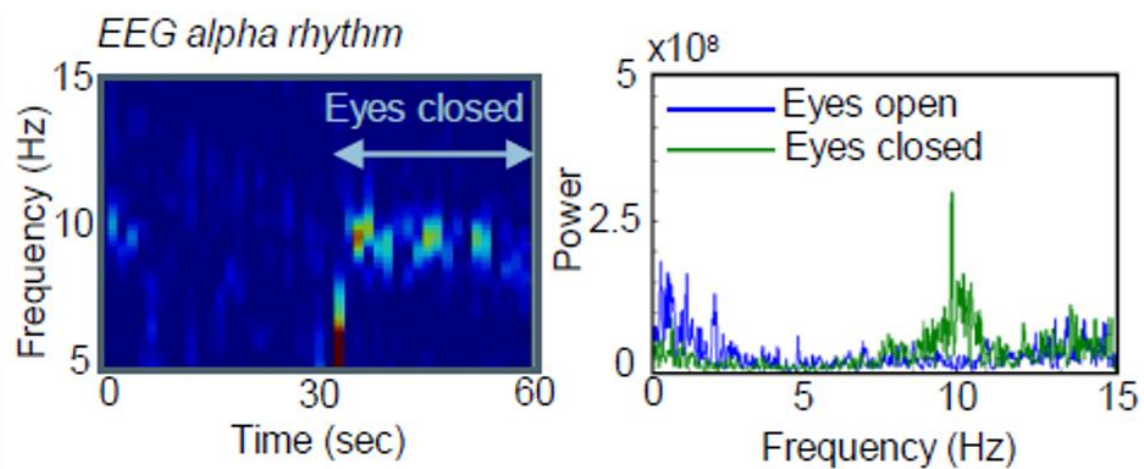


**Figure S9**

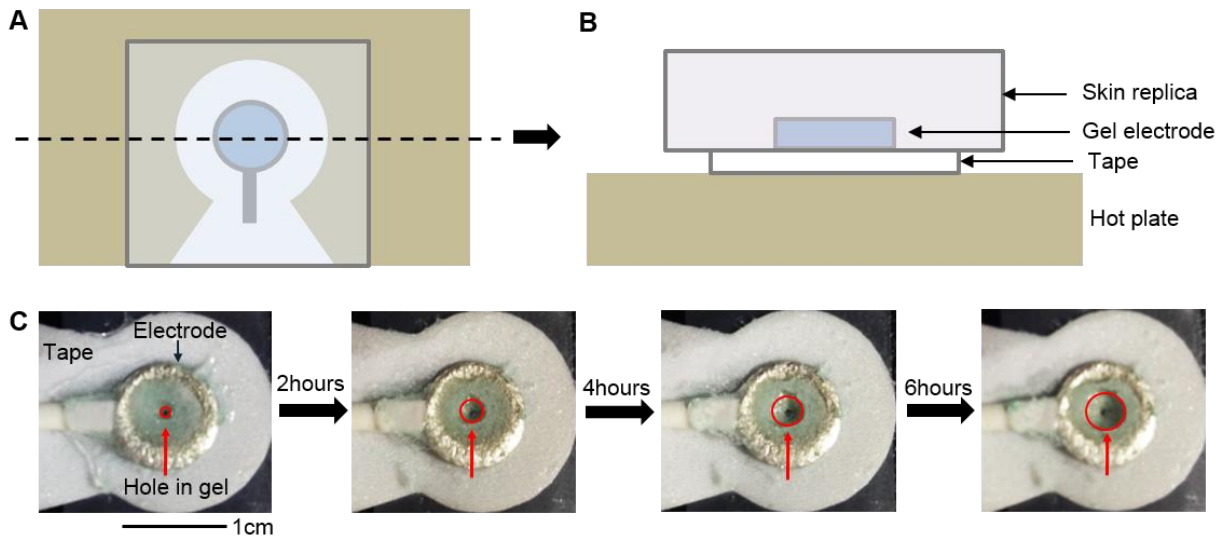


**Figure S10**

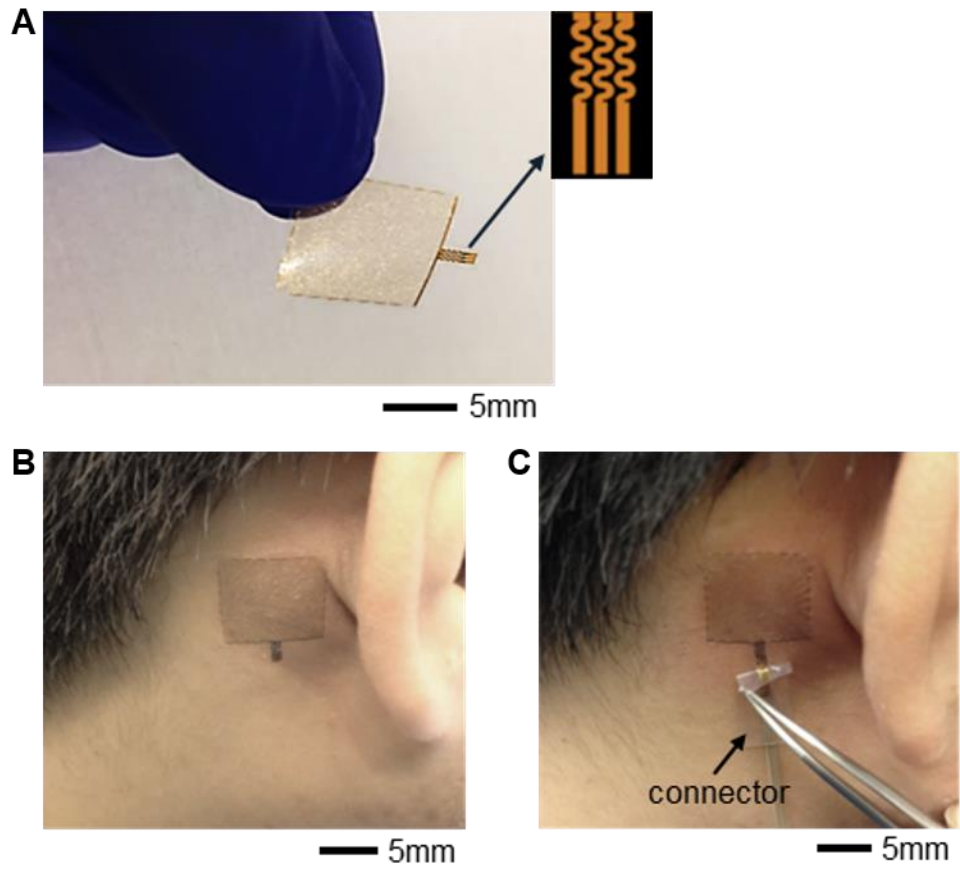


**Figure S11**

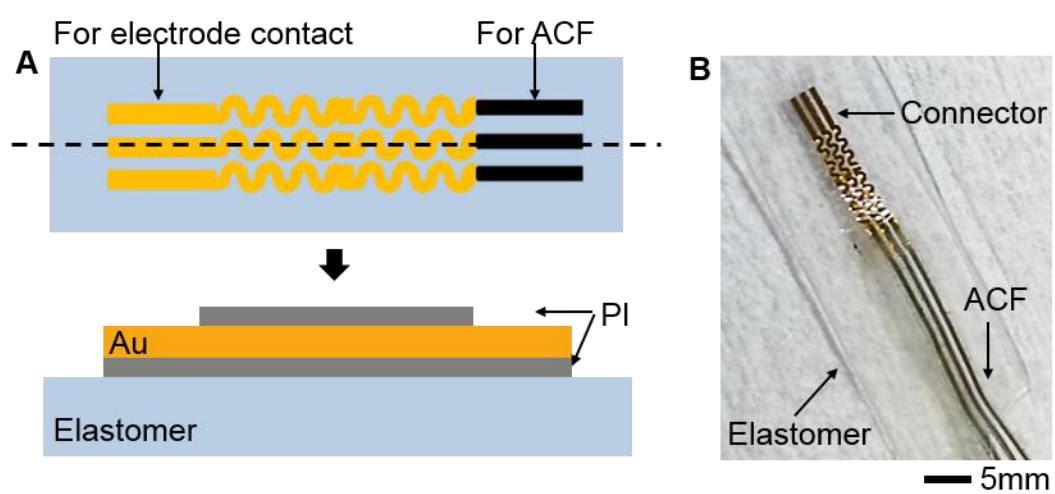


**Figure S12**

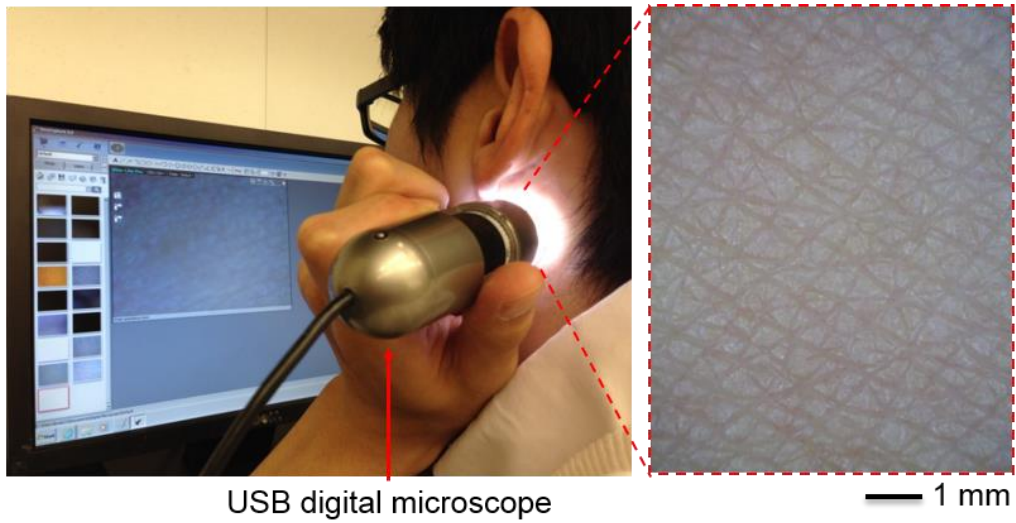


**Figure S13**

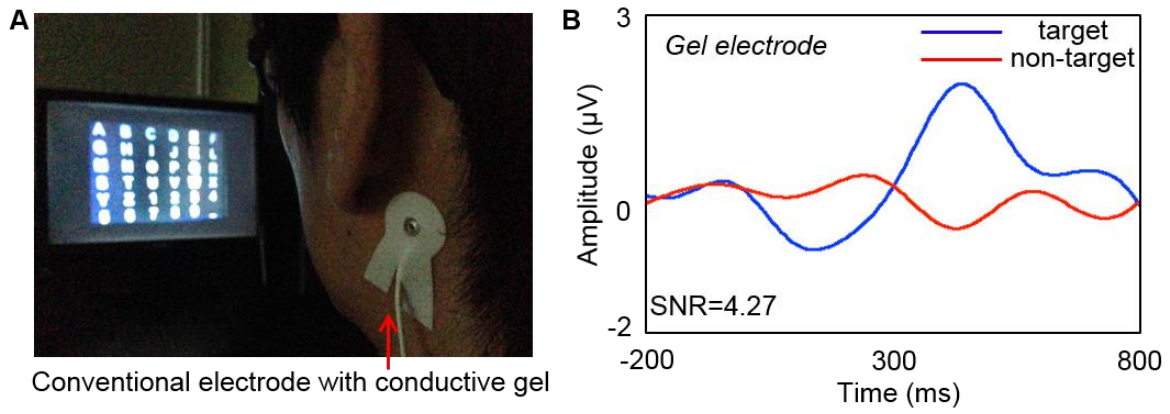


**Figure S14**

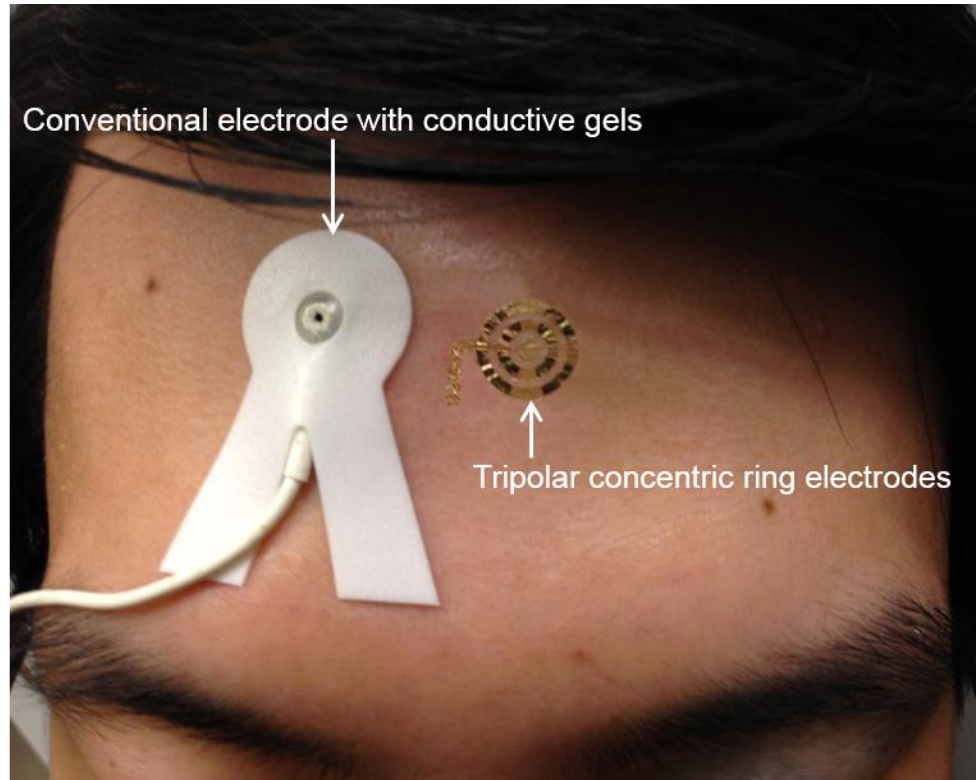


**Figure S15**

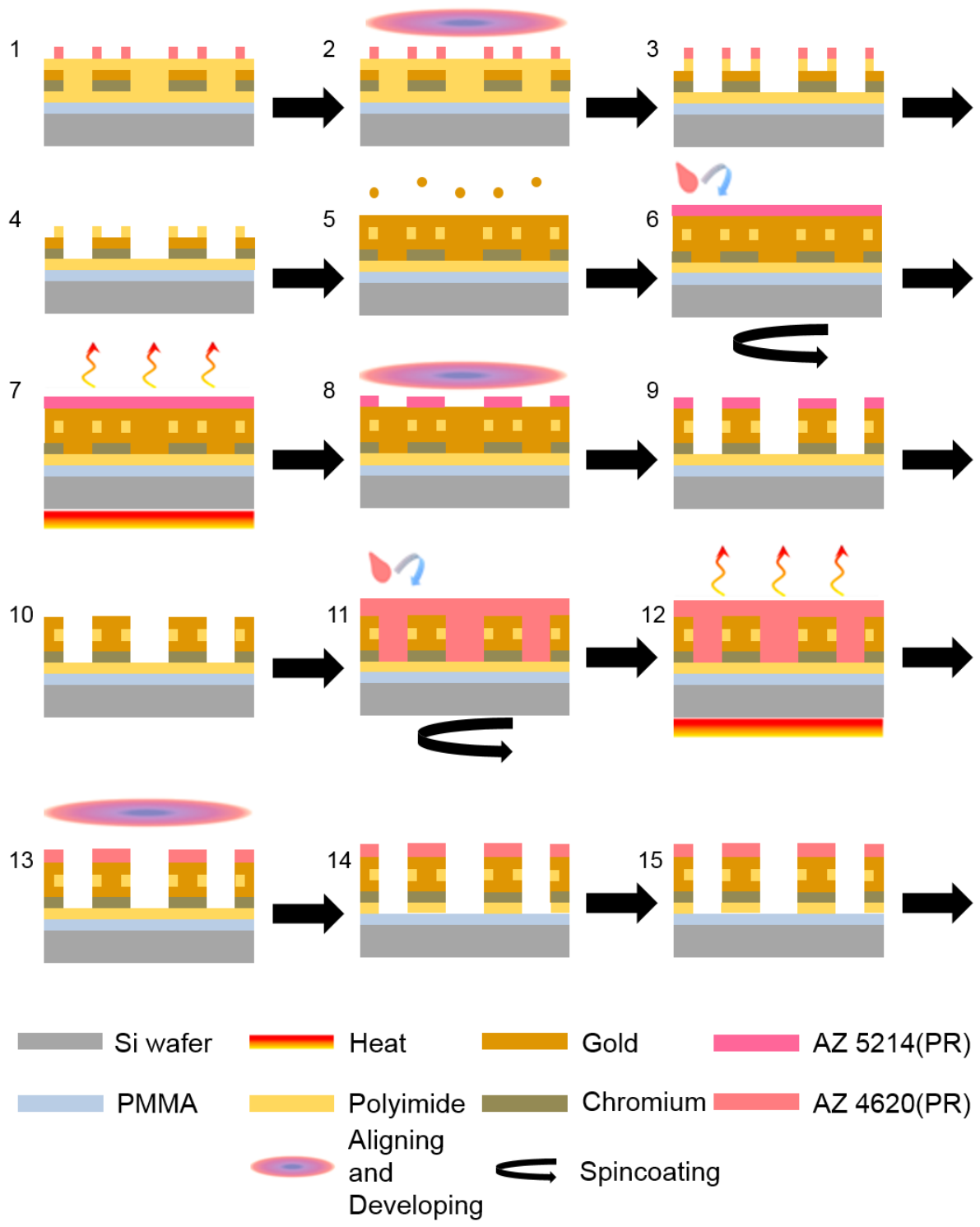


**Figure S16**

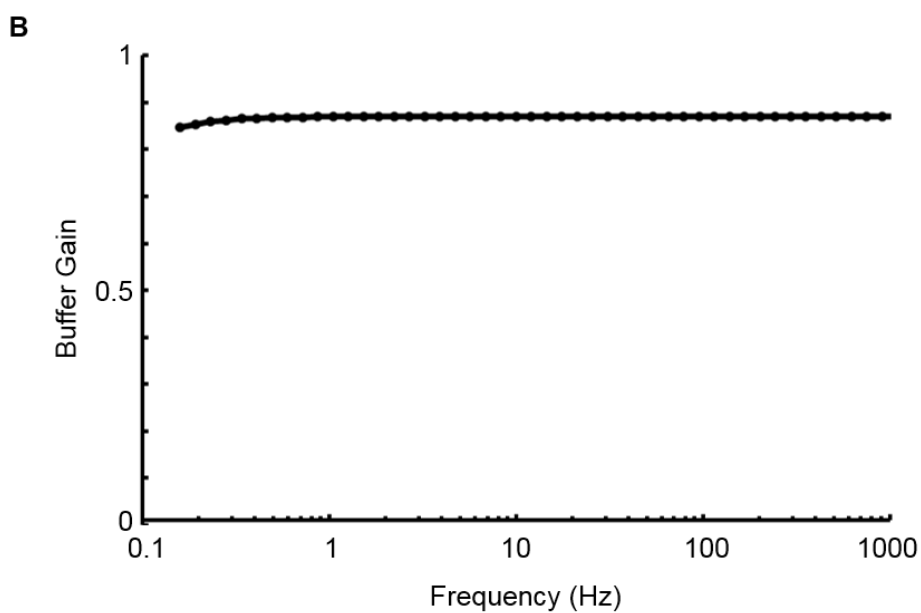
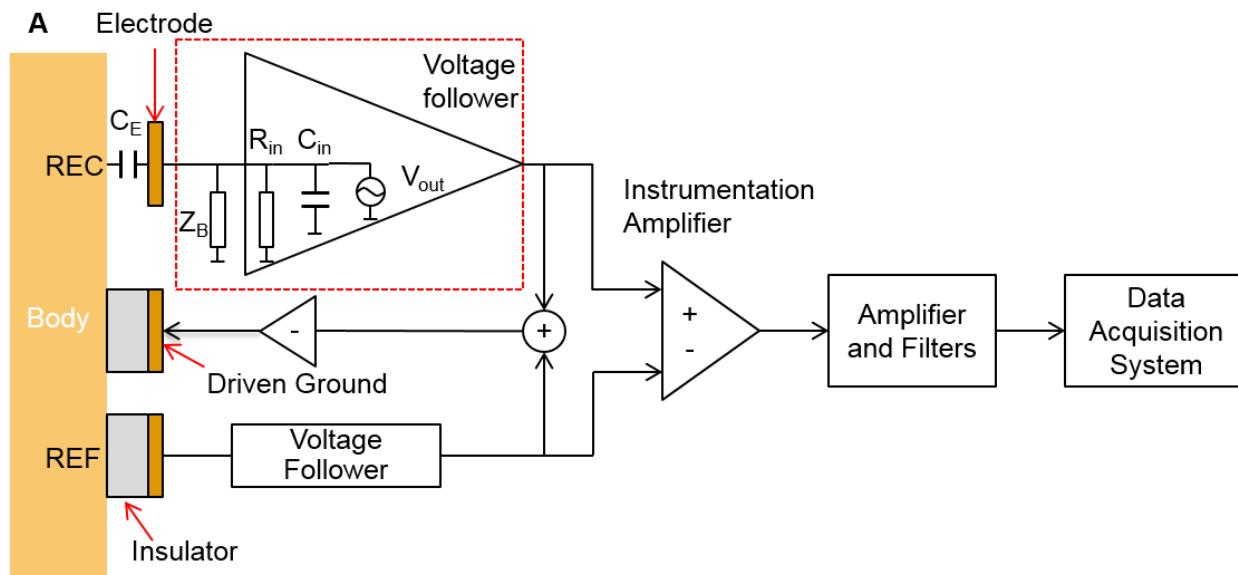


**Figure S17**